Korean J. Chem. Eng., **31**(7), 1148-1161 (2014)
DOI: 10.1007/s11814-014-0022-6

pISSN: 0256-1115
eISSN: 1975-7220

Computational fluid dynamics simulations of interphase heat transfer in a bubbling fluidized bed

Musango Lungu, Jingyuan Sun, Jingdai Wang†, Zichuan Zhu, and Yongrong Yang

State Key Laboratory of Chemical Engineering, Department of Chemical and Biological Engineering, Zhejiang University, Hangzhou 310027, China
(*Received 1 November 2013 • accepted 14 January 2014*)

Abstract−Numerical simulations based on the Eulerian-Eulerian approach have been performed in the study of interphase heat transfer in a gas solid fluidized bed. The kinetic theory of granular flow (KTGF) has been used to describe the solid phase rheology. An assessment of drag models in the prediction of heat transfer coefficients shows that no major difference is observed in the choice of the drag model used. Fluctuations of the interphase heat transfer coefficient have been found to be closely related to the bubble motion in the bed. Effects of the wall boundary condition, inlet gas velocity, initial bed height and particle size on the predicted heat transfer coefficient have also been investigated. Typical temperature profiles in the bed show that thermal saturation is attained instantaneously close to the gas distributor. Simulated results of the coefficients are in fair agreement with those reported in literature.

Keywords: CFD, Drag Model, Fluidization, Heat Transfer, Simulation

INTRODUCTION

Fluidized bed technology has found popular use in many industrial applications such as gas phase polymerization, combustion, drying operations and fluid catalytic cracking, to mention a few due to excellent solids mixing and heat transfer characteristics. These ideal characteristics are brought about by the vigorous particle motion and intimate contact of the gas and solid phases. In gas solid fluidized beds, three modes of heat transfer arise: surface-to-bed, interparticle and particle-to-gas. The majority of studies reported in literature have focused on the surface-to-bed heat transfer.

Mickley and Faribanks [1] proposed a packet or cluster renewal mechanistic model to explain the mechanism of heat transfer from the bed to the surface. Several other attempts have been made by various investigators [2,3] in the past to model heat transfer in fluidized beds using mechanistic and empirical models. However, mechanistic and empirical models have their shortcomings that render them unattractive. Mechanistic models are constrained by the assumptions on which they are based, while empirical models work well only within the range of experimental data on which the model was arrived at [4]. Furthermore empirical correlations do not help much in the understanding of the fundamental transport mechanisms [5].

The advent of high speed computers has given rise to the use of computational fluid dynamics (CFD) as an indispensable tool in the study of complex hydrodynamics and transport processes in multiphase flow systems. Based on the continuum approach, Syamlal and Gidaspow [6] used the K-FIX computer code to predict the wall to bed heat transfer coefficients in a bubbling fluidized bed. Their work revealed that it is possible to predict the large heat transfer coefficients without the use of any turbulence model. Several other studies [4,5,7,8] have been conducted to model wall to bed heat transfer in bubbling fluidized beds.

Particle-to-particle heat transfer occurs mainly due to conduction through the contact points between the particles and due to heat exchange through the gas layer separating the particles. Delvosalle and Vanderschuren [9] developed an inter-particle heat transfer model due to conduction through the gas layer between a hot and a cold particle. Chang et al. [10] modeled direct particle to particle heat transfer between different particle classes in a gas solid fluidized bed, combining the stochastic collision frequency and the direct heat conduction due to elastic deformation during impact.

Hitherto, very few detailed modeling studies have been dedicated to particle-to-gas heat transfer in fluidized bed reactors despite the fact that some industrial reactors like gas phase polymerization reactors are operated adiabatically [11] with the heat of polymerization being removed as sensible heat by the recycled gas stream. In such instances no immersed heat transfer tubes are available and so the wall to bed heat transfer in such cases is not significant. Inaccuracies in the measurement of particle and gas temperatures have made experimental determination of the particle-to-gas heat transfer coefficient difficult. Furthermore, due to the complex flow pattern in fluidized beds, the particle-to-gas heat coefficients reported in literature vary a great deal depending on the flow assumption used [12]. The amount of heat exchange between the two phases is unknown and difficult to measure or guess; thus, computational fluid dynamics can provide an insight into the heat transfer process in fluidized beds.

Kaneko et al. [13] used a discrete element method (DEM), incorporating the reaction and kinetic balances to analyze temperature behaviors of particles and gas in a fluidized bed reactor for polyolefin production. Their simulations revealed hot spot formation on the distributor near the wall of the fluidizing column. Despite the increase in computational capabilities, the current available com-

†To whom correspondence should be addressed.
E-mail: wangjd@zju.edu.cn

putation capacity renders the DEM approach less attractive in modeling dense fluidized beds such as bubbling fluidized beds. CFD simulations were carried out by Behjat et al. [14] to investigate hydrodynamic and heat transfer phenomena of a bimodal particle mixture in a gas solid fluidized bed. They assumed that solid heat conductivity includes both direct conduction through the fractional contact area and indirect conduction through a wedge of gas that is trapped between the particles. Hamzehei et al. [15] used an Eulerian-Eulerian model, incorporating the standard k-ε model turbulence model in the simulation of unsteady flow and heat transfer in a gas solid fluidized bed in which hot air entered a cold bed. Their simulation results were in close agreement with experimental data. Chen et al. [16] developed a three-dimensional computational fluid dynamics-population balance method (CFD-PBM) coupled model using an Eulerian-Eulerian two-fluid model to describe the gas-solid two phase flow in fluidized bed polymerization reactors. Their results show that the inlet gas velocity is an important parameter in controlling reactor temperature fields. As mentioned, 3-D simulations are computationally intensive for parametric studies. Accurate predictions of heat transfer coefficients are pertinent to the successful design, scale-up and operation of fluidized beds.

In the present work numerical simulations to predict heat transfer coefficients in a hot gas solid bubbling fluidized bed reactor containing linear low density polyethylene (LLDPE) particles have been performed using a verified heat transfer model [5] based on the two-fluid approach. This approach treats the gas and solid phases as interpenetrating continua. Though the two fluid model (TFM) is derived from conservation equations of mass, momentum and energy, the interphase momentum and heat exchange coefficients are empirical and hence need detailed investigation. To this effect an investigation of different drag models has been carried out to study their effect on the predicted coefficients. Influences of the inlet gas velocity, particle size and initial height on the predicted heat transfer coefficient have also been investigated. A typical temperature profile of the gas and solid phase in the reactor has been presented.

CFD MODEL

The relevant governing equations and the respective constitutive relations are given in appendix A. The viscous dissipation and work terms are small when compared to the other terms in the heat balance (accumulation, conduction, convection and interphase transfer) and have thus been omitted [7]. The interphase momentum exchange has been closed using the Syamlal O'Brien [17], Adjusted Syamlal O'Brien [18], Gidaspow [19], Cao-Ahmadi [20] and Hill-Koch-Ladd drag [21] models respectively which are given in Appendix A. The solid phase rheology has been described using the popular and well known kinetic theory of granular flow [19]. The bulk solid viscosity, which describes the resistance of the particle suspension to compression, has been modeled according to Lun et al. [22]. The shear viscosity, which is composed of three components, kinetic [19], collision [19] and friction [23], has been considered in the model. Solids pressure, which represents the normal solid phase forces due to particle-particle interactions, has been handled using the expression by Lun et al. [22], meanwhile the radial distribution function, which describes the probability of particles colliding, has been modeled according to Ma and Ahmadi [24]. The expressions just described have also been given in Appendix A. The Gunn correlation [25] recommended for granular flows has been used to close the interphase heat exchange between the two phases since it's applicable for the porosity range of 0.35-1 and a Reynolds number up to 10^5. It is well suited for fluidized bed heat transfer modeling. The next subsection reviews some available Nusselt number correlations.

1. Nusselt Number Correlations

There are numerous empirical correlations reported in literature for the estimation of both packed bed and fluidized bed fluid-to-particle heat-transfer coefficients. These correlations relate the Nusselt number to the Reynolds number, Prandtl number and in some cases the voidage. Table 1 below lists some of the correlations. The correlations have been plotted in Fig. 1 assuming a constant porosity of 0.52 and a constant Prandtl number of 0.7155, and from the figure two distinct groups can be seen. For the first group, which includes correlations due to Gunn [25], Ranz and Marshall [26] and Wakao et al. [27], the Nusselt number approaches a constant value as the Reynolds number approaches zero. For the second group con-

Table 1. Nusselt number correlations

Ranz and Marshall [26]	
Fixed bed	$Nu=2+1.8Re_s^{1/2}Pr^{1/3}$
BFB	$Nu=2+0.6Re_s^{1/2}Pr^{1/3}$
Nelson and Galloway [29]	
Fixed bed, BFB	$Nu=\dfrac{2\zeta+\left\{\dfrac{2\zeta^2(1-\alpha_g)^{1/3}}{[1-(1-\alpha_g)^{1/3}]^2}-2\right\}\tanh\zeta}{\dfrac{\zeta}{1-(1-\alpha_g)^{1/3}}-\tanh\zeta}$ where $\zeta=\left[\dfrac{1}{(1-\alpha_g)^{1/3}}-1\right]\dfrac{\varepsilon}{2}Re_s^{1/2}Pr^{1/3}$
Cybulski et al. [28]	$Nu=0.07Re_s$
Fixed bed	
Gunn [25]	$Nu=(7-10\alpha_g+5\alpha_g^2)(1+0.7Re_s^{0.2}Pr^{1/3})+(1.33-2.4\alpha_g+1.2\alpha_g^2)Re_s^{0.7}Pr^{1/3}$
Fixed bed, BFB	

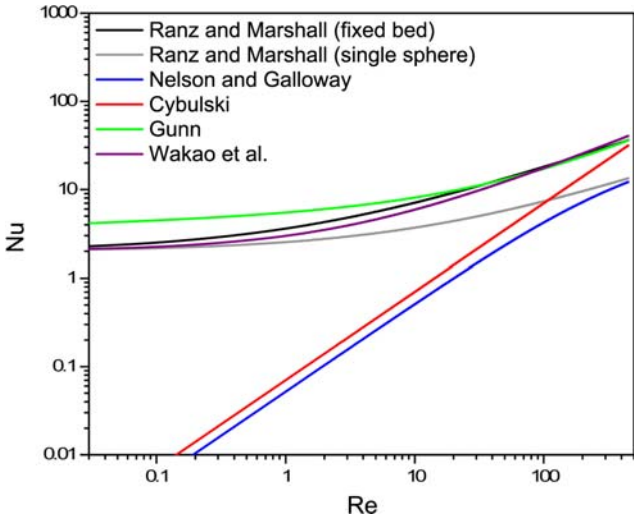

Fig. 1. Nusselt number correlations from literature.

Table 2. Simulation model parameters in Fluent 6.3

Description	Taghipour et al. [33]	Present work
Particle density	2600 kg/m^3 (glass beads)	918 kg/m^3 (LLDPE)
Gas density	1.225 kg/m^3 (air)	1.2 kg/m^3 (air)
Mean particle diameter	275 μm	348 μm
Particle heat capacity	737 J/kg·K	2600 J/kg·K
Gas heat capacity	1006.43 J/kg·K	994 J/kg·K
Particle thermal conductivity	1.0 W/m·K	0.29 W/m·K
Gas thermal conductivity	0.0242 W/m·K	0.00257 W/m·K
Initial particle temperature	300 K	313 K
Initial gas temperature	300 K	353 K
Static bed height	0.4 m	0.3 m
Bed porosity	0.4	0.52
Bed width	0.28 m	0.15 m
Bed height	1.0 m	1.0 m
Superficial gas velocity	0.46 m/s ($7U_{mf}$)	0.22-0.66 m/s ($2U_{mf} - 6U_{mf}$)

sisting of correlations due to Cybulski et al. [28] and Nelson and Galloway [29], the Nusselt number approaches zero as Reynolds number approaches zero, and this is attributed to the negligence of axial dispersion [25]. However, for an isolated sphere in an infinite stagnant fluid the theoretical limiting value of the Nusselt number is 2 [30]; thus the second group are not suitable as they predict Nu numbers less than the theoretical minimum with decreasing Re number. From the first group to which the Gunn correlation belongs we observe that correlations due to Ranz and Marshall and Wakao et al. approach the limiting value of 2 well before the Gunn correlation does, implying that the Gunn correlation can be used for a wider range of Re. The Gunn correlation is applicable for a porosity range of 0.35-1 and for Re up to 10^5 as was aforementioned in section 2 of the manuscript, making it ideal for simulations involving heat transfer in fluidized beds. In addition, the Gunn correlation satisfies several other less evident asymptotic conditions [5]. Recently, Kuiper's research group in the Netherlands validated the Gunn correlation using DNS simulations [31]. The agreement between the fitted heat transfer coefficients and the results obtained from the empirical correlation of Gunn were quite reasonable, especially at the higher Reynolds numbers.

SIMULATION SETUP

The geometry used in the simulations is a 2D fluidized bed which is the same as that used by Sun et al. [32]. The bed has a diameter of 15 cm and height of 100 cm. The grid is created in GAMBIT 2.3.16 and exported into FLUENT 6.3.26, a CFD commercial software package used to execute the numerical simulations. The grid is a uniform quadratic mesh with 5 mm size interval in both the radial and axial directions, thus giving 6000 computational cells. An initial sensitivity study revealed that this mesh size is sufficient for an independent mesh solution. Linear low density polyethylene (LLDPE) is used as the granular media and air as the fluidizing medium. The minimum fluidization of the particles is 0.11 m/s, while the porosity of the bed at minimum fluidization is 0.52. The properties of the gas and solid phase are given in Table 2 below.

Experimental voidage data from the work of Taghipour et al. [33] was used to validate the model used in the present work. They conducted experiments in a pseudo 2D using air and glass beads of 250-300 mm diameter (classified as Geldart B). Similarly, LLDPE parti-

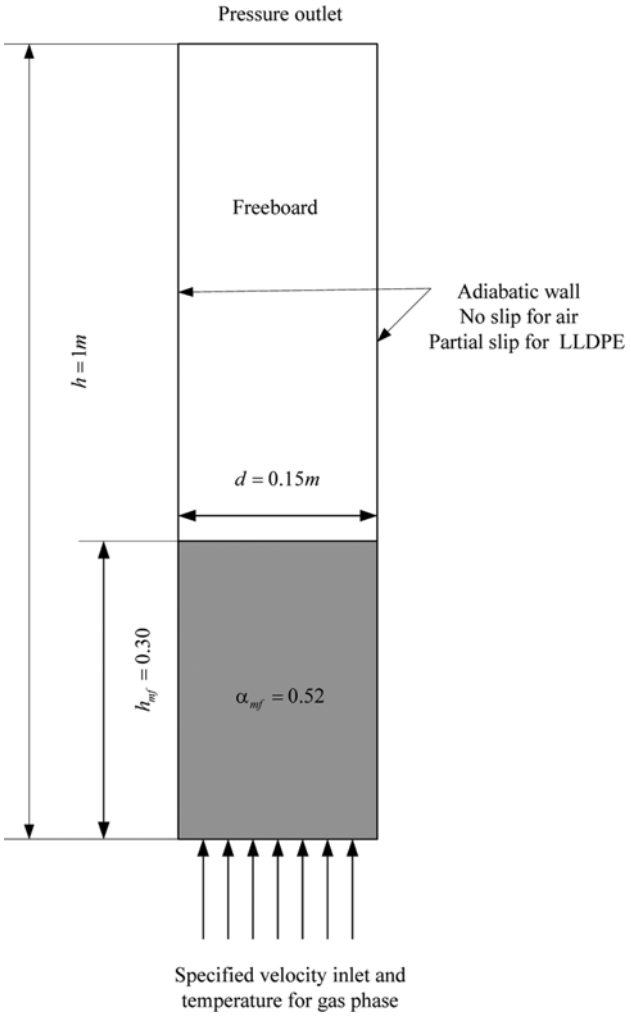

Fig. 2. Geometry of simulation system with boundary conditions.

cles are classified as Geldart B, and thus the fluidization behavior in the system reported in [33] is supposed to closely resemble that being simulated. Detailed simulation parameters from Taghipour et al. have also been listed in Table 2 below.

1. Boundary and Initial Conditions

The initial condition of minimum fluidization is used for all the simulations. At the bottom of the bed a uniform velocity inlet and temperature is specified for the gas phase only, as no solids enter the computational domain. At the top of the column a pressure outlet boundary condition is assigned. The left and right walls are designated as no slip for air, and the partial slip wall boundary condition of Johnson and Jackson [34] has been adopted for the particulate phase with a specularity coefficient of 0.5, which is commonly used in simulating bubbling fluidized beds [35]. In addition, the thermal energy boundary condition at the walls is set to adiabatic. Initial values of the pressure profile, solid volume fraction and temperatures are patched in the flow field. Fig. 2 below gives a summary of the geometry, initial and boundary conditions used.

2. Simulation Procedure and Method

The simulations were run for 20 seconds real time in the unsteady state mode and quantities were time averaged for the last 15 seconds as it took 5 seconds for the initial start-up effects to subside. Second-order spatial discretization was used for momentum, granular temperature and energy, second-order implicit for the transient formulation and the QUICK scheme for volume fraction. For pressure velocity coupling the semi implicit method for pressure linked equations (SIMPLE) scheme was used. A fixed time step of 0.0005 s was used throughout the simulations. The default convergence criteria of 10^{-3} were used for all quantities except for the energy equations, which were set to 10^{-6}.

RESULTS AND DISCUSSION

1. Mesh Refinement Study

Investigation of the effect of the mesh size on the solution results is one of the first steps performed in CFD studies. Ideally a mesh independent solution is one which does not change with further mesh refinement. Grid sensitivity was carried out with interval spacing of 2.5 mm, 5 mm and 10 mm, respectively, in both the radial and axial direction corresponding to 24000, 6000 and 1500 grids, respectively. Fig. 3 shows the time averaged (5-20 sec) and spatially averaged (along the width of the reactor) volumetric interphase heat transfer coefficient profile along the height of the reactor obtained using the three mesh sizes. Qualitatively, all three mesh sizes give a similar trend. Calculated average values of the coefficients show that grids of size 24000 and 6000 give nearly the same value, indicating that a mesh size of 5 mm gives a grid independent solution. Table 3 shows the calculated average values of the transfer coefficient in the bed.

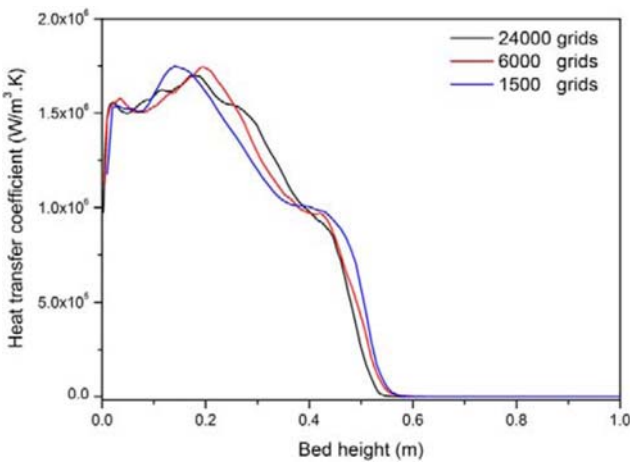

Fig. 3. Time averaged interphase heat transfer coefficient for different grid resolution (U_g=0.44 m/s, Hill et al. drag model).

Table 3. Average interphase heat transfer coefficient for different number of grids

Number of grids	Predicted heat transfer coefficient ($W/m^3 \cdot K$)
24000	663624.44
6000	664145.58
1500	659973.79

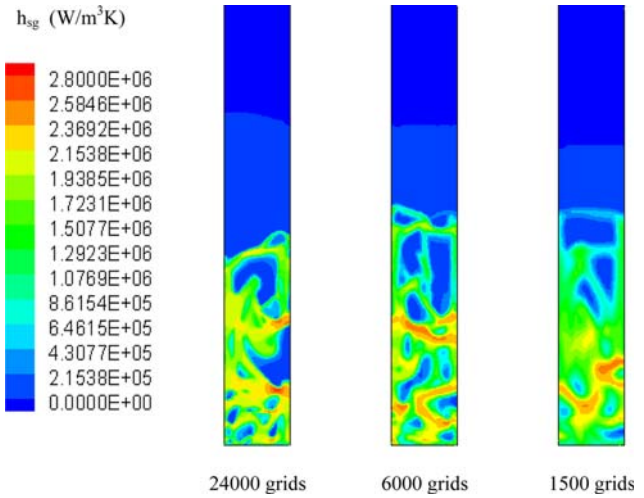

Fig. 4. Contours of the interphase heat transfer coefficient for different mesh resolutions (U_g=0.44 m/s, t=20 seconds).

Fig. 4 gives the instantaneous heat transfer coefficient in the bed after 20 seconds and at a velocity of 0.44 m/s. The figure further confirms that meshes with 24000 and 6000 grids show similar characteristics in the dense bed. Consequently, a mesh with 6000 grids was adopted and used in the remainder of the studies.

2. Drag Model Study

2-1. Qualitative Comparison of Drag Models

The observed high heat transfer rates in fluidized bed reactors are attributed to the hydrodynamics [36]. The drag force plays an important role in influencing the hydrodynamics in the fluidized bed and therefore needs investigation. Fig. 5 shows the contour plots of the solids volume fraction obtained using different drag models after 20 seconds of simulation and at a superficial gas velocity of 0.44 m/s. Clearly, all the models give a similar qualitative result with respect to bed expansion and bubble shape. At 20 seconds the bed is already at steady state and thus the contour plots represent the typical fluidization behavior in the bed. A comparison between the adjusted Syamlal O'Brien and Syamlal O'Brien models reveals that the former predicts a slightly higher bed expansion and smaller average bubble size compared to the latter. Small bubble size translates to slower bubble rise velocity, and consequently a higher expanded

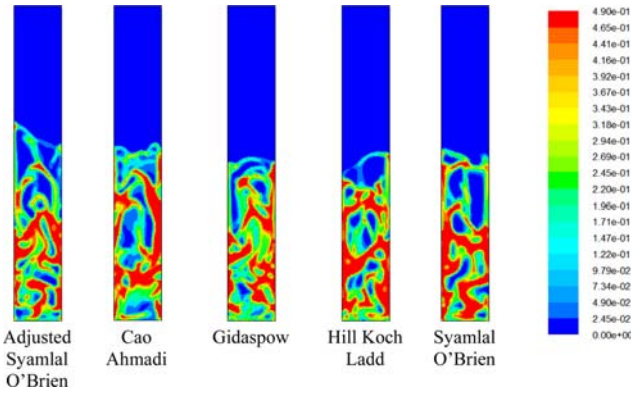

Fig. 5. Contours of the solid volume fraction for different drag models (U_g=0.44 m/s, t=20 s).

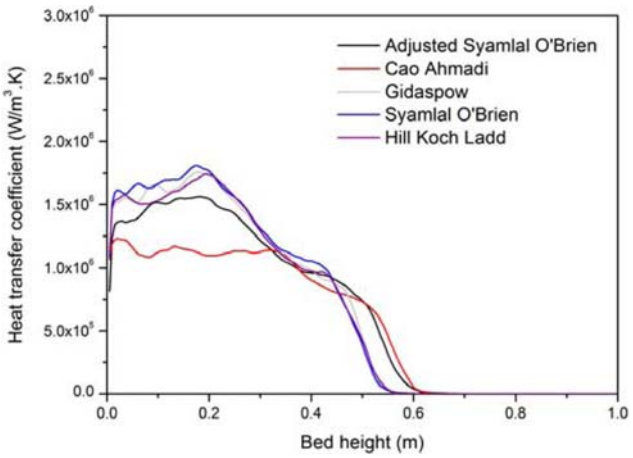

Fig. 6. Comparison of interphase heat transfer coefficient profiles for different drag models (U_g=0.44 m/s).

bed height [37]. Generally, smaller bubbles can be observed close to the plate distributor and large bubbles are visible at higher heights near the freeboard for all the drag models. This is in agreement with the experimentally observed trend that bubbles grow as they rise in the bed due to coalescence.

Although there have been extensive comparisons of drag models in hydrodynamics [38,39], parallel work for heat transfer modeling in fluidized beds is scanty [40]. Fig. 5 shows a plot of the time averaged (5-20 sec) and spatially averaged (along the width of the reactor) volumetric interphase heat transfer coefficient profile along the height of the reactor obtained using different drag models at a superficial velocity of 0.44 m/s. The heat transfer coefficients were calculated using a user-defined function incorporated into FLUENT 6.3.26 and the simulation data was exported into Matlab for processing. Qualitatively, all drag models give a similar trend in the interphase heat transfer coefficient profile.

All the drag models show that near the inlet of the bed the heat transfer coefficient rises sharply at first, reaching a characteristic peak and then varies unsteadily until about a height of 0.45 m, after which it then starts to decline gradually until it reaches zero. The Cao Ahmadi drag model predicts the least value of the coefficient in the dense phase and the largest in the lean phase. Relative to other models the Cao Ahmadi model predicts a large voidage in the dense bed from a plot of spatially and time averaged bed voidage for different drag models (available on demand), which is not presented in the paper to avoid repetition of data and for the sake of brevity. A higher voidage means that heat transfer is poor, and thus the observed low heat transfer coefficient profile in the dense bed. In bubbling fluidized beds particles are seldom blown out of the reactor and thus a reduction of particle concentration in the dense phase leads to a corresponding increase in the upper part of the reactor and thus the observed high heat transfer coefficient predicted by the Cao Ahmadi drag model in the lean phase. When the Syamlal O'Brien model is adjusted to predict the experimentally observed minimum fluidization velocity, it is observed that the resulting model (adjusted Syamlal O'Brien) predicts a reduced value of the heat transfer coefficient in the dense bed and a corresponding increase in the lean phase. As aforementioned, the adjusted Syamlal O'Brien model predicts an expanded bed height, which results in the reduction of particle concentration in the dense bed and a corresponding particle concentration increase in the upper part of the reactor due to the slow rising bubbles. Since the volumetric interphase heat transfer coefficient is directly proportional to the solid volume fraction, it will exhibit a similar behavior to the particle concentration profile.

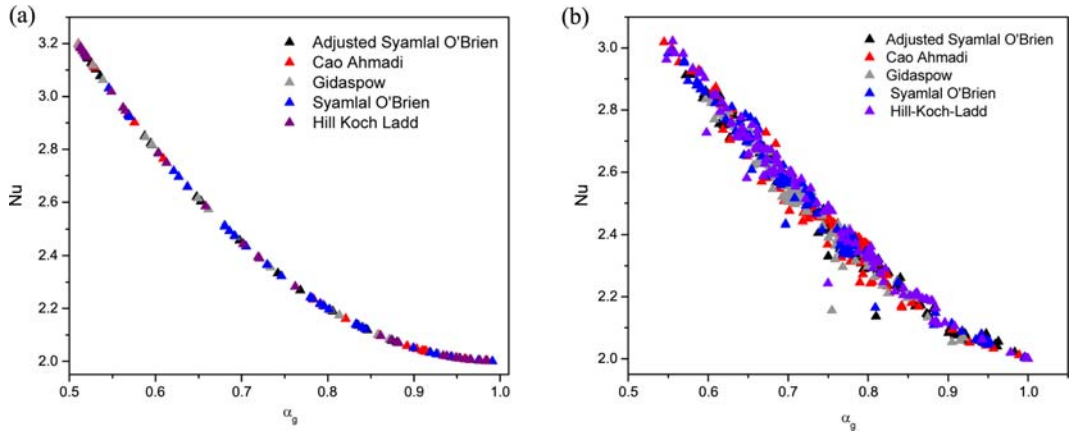

Fig. 7. Plot of (a) local Nu number dependence on voidage for different drag models at a height of 0.3 m above the plate distributor at 20 s (b) time and spatially averaged Nu number dependence on voidage in the fluidized bed.

In addition, small bubble sizes in gas solid fluidized beds seem not to enhance solids mixing, which results in the observed low heat transfer coefficient in the dense phase. The Gidaspow, Syamlal O'Brien and Hill Koch Ladd drag models predict similar profiles of the heat transfer coefficient along the height of the reactors which are all close to each other with insignificant differences. In bubbling fluidized beds the lean phase contains very few solid particles or none at all; therefore, the heat transfer coefficient drops to zero, indicating that gas (air) is a poor transporter of heat as shown by Eq. (A.40).

Fig. 7 displays local and time-averaged plots of the Nu dependence on voidage for different drag models. As expected, the drag models have very little influence on the predicted profiles. Both the local and time-averaged plots display similar characteristics of exponential decay with increasing voidage. At low voidage the Nusselt number is high, and consequently higher heat transfer coefficients are predicted. Typically, low voidage exists in the dense region of the bubbling fluidized bed, and it is in this region that high heat transfer rates are experienced. As the voidage approaches one, the Nusselt number approaches the limiting value of two.

2-2. Quantitative Comparison of Drag Models

The time-averaged voidage predicted by the various drag models has been compared against experimental data reported by Taghipour et al. [33] From Fig. 8, the simulated result of the time averaged voidage profile at a height of 0.2 m above the distributor plate at a gas velocity of 0.46 m/s compares fairly well with the experimental data. Both the simulated and experimental results show that the voidage in the core of the bed is high with a slight decrease near the wall. This profile correctly demonstrates that preferred path of the bubbles in the center of the bed. Cao Ahmadi predicts the largest value of the time-averaged voidage along the whole radial distance of the bed. The adjusted Syamlal O'Brien gives the second largest value of the voidage but only on the left plane of the reactor. On the right plane it gives similar results to other drag models. The Syamlal O'Brien model gives good results in comparison to the experimental data near the walls but not in the core of the bed. The Hill Koch Ladd model predicts consistent and nearly symmetrical values of the voidage in the core of the bed. Overall, the differences between

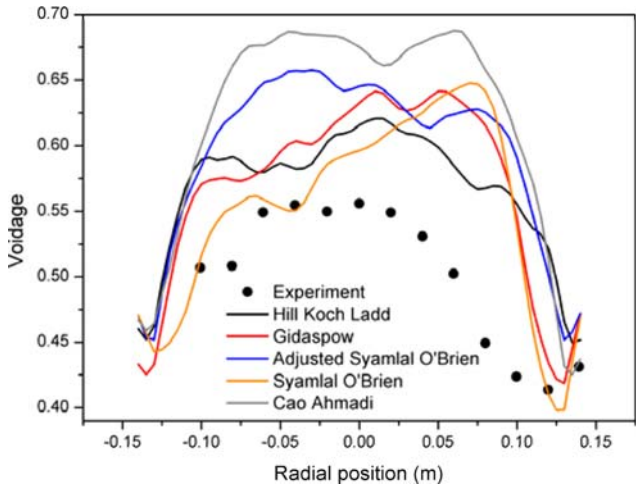

Fig. 8. Experimental and Simulated time averaged voidage profile at a height of 0.2 m above the distributor and superficial gas velocity of 0.46 m/s.

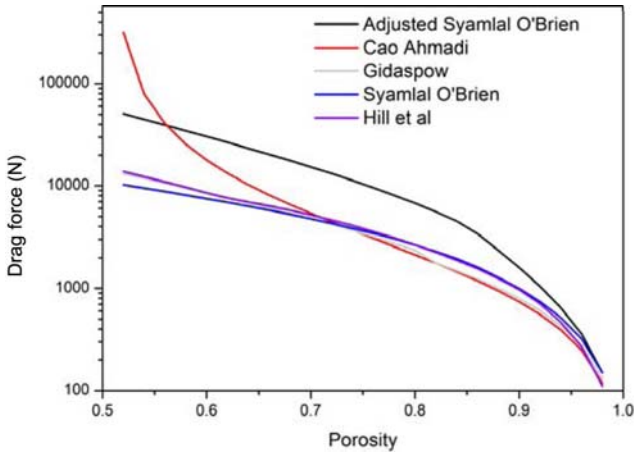

Fig. 8. Drag force for different drag models as a function of porosity for the conditions listed in Table 2.

the drag models are not very large. Consequently, the Hill Koch Ladd drag model was adopted and used in the rest of the simulations.

Fig. 8 is a plot of the drag force as a function of the porosity for different drag models at a relative velocity of 1m/s. The drag force, which is a function of the porosity, slip velocity and properties of the gas and solid phase, has been calculated using the conditions listed in Table 1. For bubbling fluidized beds the mean voidage range is 0.45 to 0.65 [41]; however, in our study we investigated the behavior of the drag correlations over a wider range from a minimum porosity of 0.52 representing packed bed to a maximum porosity of 0.95. From the plot it is clear that the shape of the drag force profile predicted by the Cao Ahmadi correlation differs from the rest. The shape of the curve resembles the letter S rotated 90° anticlockwise. At the minimum fluidization condition, the Cao Ahmadi model predicts the largest drag force and with increasing porosity it decreases and crosses the Adjusted Syamlal O'Brien at a porosity of 0.56 and the other drag models between the porosity ranges of 0.7 to 0.82 after which it gives the least value. The Gidaspow, Syamlal O'Brien and the Hill Koch Ladd drag models show a similar behavior throughout the whole porosity range and give values close to each other with the drag force reducing with increasing bed voidage. A closer look at the Gidaspow model reveals a 'switch' inherent in the drag model at a porosity of 0.8. The drag force predicted by the three drag models is significantly lower than that predicted by the adjusted Syamlal O'Brien drag model. This is in agreement with Vejahati et al. [39] who observed that adjustment of drag models based on the minimum fluidization velocity results in prediction of higher values of drag coefficient and consequently drag force throughout the whole porosity range. In conclusion, the drag model study shows that very minor differences are observed with the choice of the drag model used for simulating heat transfer in the gas solid bubbling fluidized bed.

The average bed volume fraction in bubbling beds can be conveniently obtained from the relationship:

$$-\frac{dp}{dy}=\rho_s(1-\alpha_g)g \tag{1}$$

From which in turn the average specific area $6\alpha_{s,ave}/d_s$ can be esti-

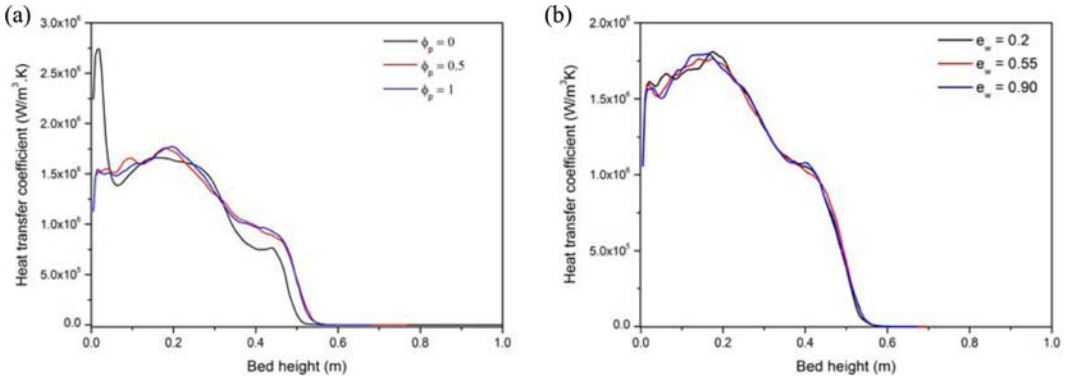

Fig. 9. (a) Heat transfer coefficient profile for different specularity coefficients, (b) heat transfer coefficient for different particle-wall restitution coefficient.

mated assuming the particles are spherical. From our simulation the average specific area was estimated to be 7,049 m^2/m^3 at a superficial gas velocity of 0.44 m/s using the Hill Koch Ladd drag model. High heat transfer rates in fluidized beds are mainly due to the large interfacial area, typically in the range of 3,000-45,000 m^2/m^3 as opposed to the low particle-gas heat transfer coefficients, which are typically in the range of 6-23 W/m^2K [42]. Our simulation predicted an average interphase heat transfer coefficient of 664 145 W/m^3K at a velocity of 0.44 m/s. From this value, the predicted *particle-to-gas* heat transfer coefficient is only 94.22 W/m^2K.

3. Effect of Wall Boundary Condition on the Predicted Heat Transfer Coefficient Profile

As has been mentioned, the wall boundary condition is taken care of using the Johnson and Jackson semi empirical equation. To investigate this effect, two parameters were varied: the specularity coefficient, ϕ_p and the particle wall restitution coefficient, e_w. The specularity coefficient is a measure of fraction of collisions which transfer momentum to the wall and assumes values between zero and one with zero indicating perfectly specular collisions and one perfectly diffuse collision. In our study ϕ_p values of 0, 0.5 and 1 representing free slip, partial slip and no slip conditions were tried. Meanwhile, e_w characterizes the dissipation of solid kinetic energy by collisions with the walls. Values of 0.2, 0.55 and 0.9 were used to investigate e_w. Fig. 9(a) shows the time averaged (5-20 sec) and spatially averaged (along the width of the reactor) volumetric interphase heat transfer coefficient profile along the height of the reactor obtained using the three slip conditions. Clearly, the free slip condition is different from the partial slip and no slip conditions, which result in similar profiles of the transfer coefficient. The free slip condition entails that the contact between the solid and the wall is frictionless, leading to higher downward solid concentration and higher velocity close to the wall [35]. This leads to accumulation to solids at the bottom of the reactor, and consequently a higher heat transfer coefficient is observed. The increase of solid particles in the bottom of the reactor is accompanied by a corresponding decrease of particle concentration in the upper part of the reactor and hence the observed reduced heat transfer coefficient in the upper part of the reactor. The absence of friction in the modeling studies leads to a different solids circulation pattern [43], which in turn affects the heat transfer coefficient profile in the bed. The partial slip and free slip conditions give nearly identical profiles of the heat transfer coefficient. Inclusion of friction leads to a reduction of the solids concentration and velocity near the wall since particles experience resistance to movement. This action leads to less accumulation of solid particles at the bottom of the reactor and therefore a lower heat transfer coefficient. At the upper part an increase of the heat transfer coefficient is observed that obviously is as a result of an increase in the particle concentration. Therefore, to predict accurate values of the heat transfer coefficient, care must be taken in the specification of wall boundary conditions.

Fig. 9(b) shows the time and spatially averaged heat transfer coefficient at a velocity of 0.44 m/s and e_w values of 0.2, 0.55 and 0.9. No apparent differences in the profiles are observed for the three e_w values, meaning that the particle wall coefficient of restitution has no effect on the model results. Similarly, Li et al. [35] did not observe any appreciable difference in the hydrodynamic behavior using different e_w values in their study. Consequently, a specularity coefficient of 0.5 and a particle wall coefficient restitution of 0.2 were used throughout our simulations.

4. Heat Transfer Coefficient Fluctuations

The transient heat transfer coefficient exhibits oscillatory behavior similar to the commonly encountered pressure fluctuations in fluidized beds owing to the bubble motion in the bed. "Numerical probes" were positioned at heights of 0.15 m, 0.30 m, and 0.45 m above the distributor to follow the time evolution of the heat transfer coefficient. As the rising bubbles approach the probe, the interphase heat exchange coefficient drops sharply due to low thermal conductivity and heat capacity of the gas phase. As the bubbles further rise, the interphase heat transfer coefficient sharply rises behind the bubbles due to the increased particle concentration in the wake. This mechanism continues, thus giving rise to the oscillatory behavior. Experimental studies with single bubbles rising in a gas-solid fluidized bed have shown that the bubble wake plays an important role in particle circulation and heat transfer [44]. The same mechanism is at play in gas solid fluidized beds with multiple bubbles. Using spectral analysis, the heat transfer coefficient fluctuations can be analyzed to obtain the dominant frequency. The dominant frequency is the highest power intensity in the PSD and is found to correspond to different mechanisms or hydrodynamic behavior variation including bubbles formation and eruption [45]. Fig. 10 shows the local instantaneous heat transfer coefficient fluctuations and the corresponding power spectral density (PSD) at heights of 0.15 m,

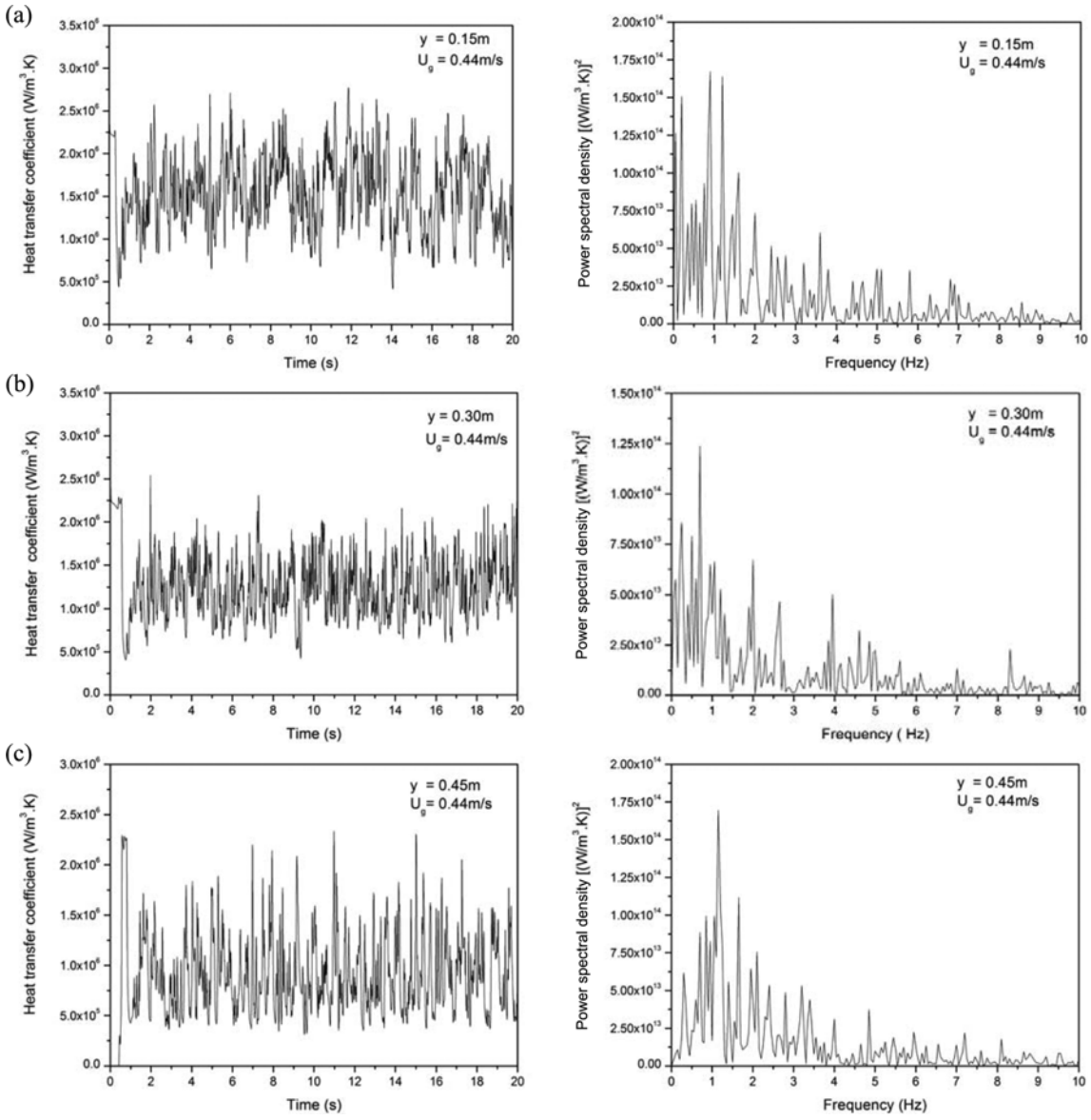

Fig. 10. Time series of the heat transfer coefficient fluctuations and corresponding power spectral density at a height of (a) 0.15 m (b) 0.30 m and (c) 0.45 m above the distributor.

0.30 m and 0.45 m above the distributor. The PSD is obtained directly from the heat transfer coefficient data using the fast Fourier transform (FFT) technique. From the figure a broad band of peak frequencies can be observed between 0 and 2.5 Hz with a dominant frequency of about 0.9 Hz. At a height of 0.15 m, the dominant frequency is not very visible as the position is closest to the distributor where the bubbles formation occurs, but with an increase in the distance from distributor the dominant frequency becomes distinct. Baskakov et al. [46] derived a formula for the natural frequency in a bubbling fluidized bed, which is the frequency associated with a single mechanism such as particle vibration or spontaneous bed oscillation. The formula is given as $f=(1/\pi)\sqrt{g/H_{mf}}$, where g is the acceleration due to gravity and H_{mf} is the bed height at minimum fluidization. Plugging in the variables yields a natural frequency of 1.82 Hz, which is larger than the dominant frequency. The dominant frequency of the local heat transfer coefficients is

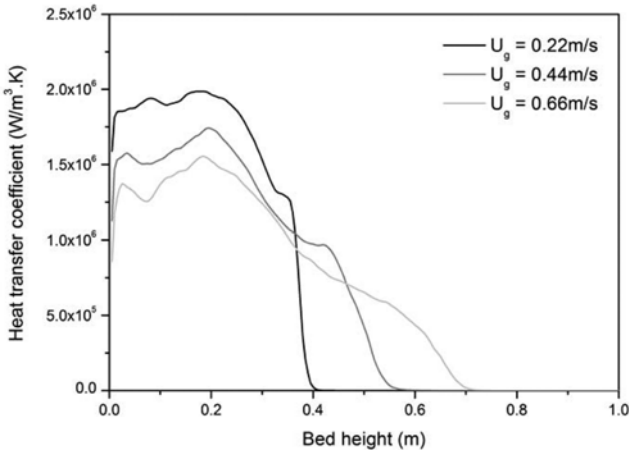

Fig. 11. Effect of the superficial gas velocity on the predicted heat transfer coefficient.

lower than the natural frequency. Therefore, a single oscillation mechanism cannot be responsible for the local fluctuations, which further proves that the heat transfer coefficient fluctuations are associated with the bubble motion in the bed.

5. Effect of Superficial Gas Velocity

Fig. 11 shows the time-averaged profile of the volumetric interphase heat transfer coefficient along the height of the reactor obtained at different superficial gas velocities. Velocities of 0.22 m/s, 0.44 m/s and 0.66 m/s which correspond to $2U_{mf}$, $4U_{mf}$ and $6U_{mf}$ have been used in the present study. An increase in velocity results in the reduction of the particle concentration in the lower part of the reactor and a corresponding increase in the upper part. From the Gunn correlation we can deduce that an increase in the void fraction leads to a reduction in the Nusselt number, and consequently the heat transfer coefficient and vice versa. As the velocity is increased from $2U_{mf}$, $4U_{mf}$ and $6U_{mf}$, the average heat transfer coefficient increases from 659 288.66 W/m^3·K, 664 145.58 W/m^3·K and 667 407.63 W/m^3·K respectively. Though a higher superficial velocity results in increased bed voidage, it also leads to higher particle Reynolds number, which enhances heat transfer in the bed. The difference in the three values is quite small due to the opposing effects of the bed voidage and the high particle Reynolds number at higher velocities.

6. Effect of the Particle Size

Fig. 12 illustrates the effect of the particle size on the predicted heat transfer coefficient at a constant superficial gas velocity of 0.44 m/s. Two particle sizes of 223 μm and 631 μm have been used in addition to the default particle size of 348 μm. An increase in the particle size results in the reduction of the heat transfer coefficient as well as the bed height. A small particle size leads to an increase in the drag force, which explains the increase in the bed height with a decrease in the particle size. The expanded bed height influences the gas residence time and ultimately the predicted heat transfer coefficient. Fig. 13 shows the drag force as a function of the voidage for the three particle sizes at a relative velocity of 1 m/s. The difference in the drag force experienced by the three particle sizes is more pronounced at lower void fractions that are in the dense bed, and this is expected since the interstitial velocity is high due to the smaller voidage and the particle movement is restricted. Note that the drag force is based on a unit volume. The drag force is reduced with increasing porosity as the particles become more mobile. As

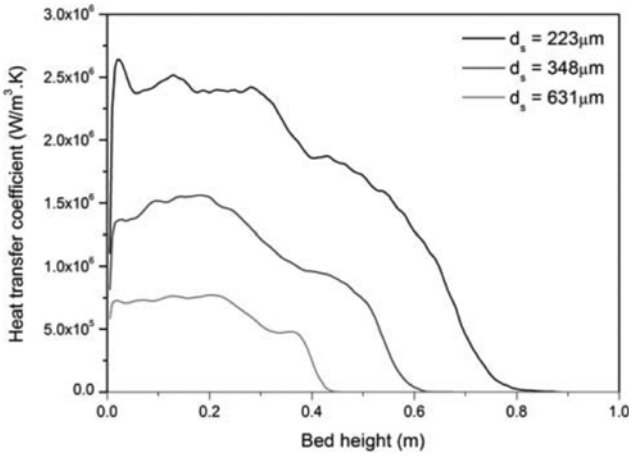

Fig. 12. Effect of particle size on predicted heat transfer coefficient.

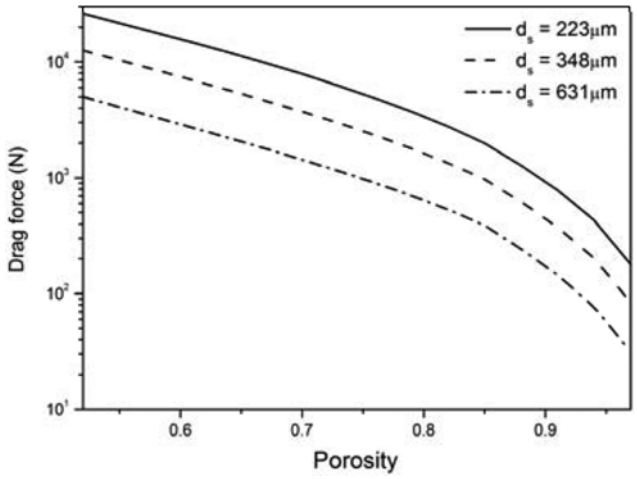

Fig. 13. Drag Force for different particle sizes.

[47,48] have demonstrated, a small particle size creates larger bubbles. Wang et al. [49] using acoustic emission (AE) investigated the influence of particle size on the flow structure in fluidized beds, and they concluded that fluidization with small particles leads to more gas bubbles being formed at the distributor, causing a larger bed expansion.

7. Effect of Initial Bed Height

The effect of the initial bed height was investigated using bed heights of 0.15 m, 0.30 m and 0.45 m respectively. Table 3 shows the values predicted for average heat transfer coefficient, height of expanded bed, expansion bed ratio, and average bed solid volume fraction and gas residence time at the three initial bed heights.

The gas residence time can be conveniently calculated from the expression [50]:

$$t_{res} = \frac{H_{exp}}{U_g / \alpha_{g,ave}} \tag{2}$$

From the table we notice that a decrease in the initial bed height results in an increase in the bed expansion ratio and a decrease in the gas residence time. In bubbling fluidized beds, the bubble rise velocity increases with an increase in the bubble diameter based on the simple two phase theory of Davidson and Harrison [12] as the bubbles move up the bed. Thus, a reactor with a small initial static bed height will have a smaller average bubble size and a high bed expansion ratio [50] as a result of the slow bubble rise velocity. A high bed expansion ratio is synonymous with an average high void fraction and thus a reduced volumetric interphase heat transfer coefficient. Thus, to promote heat transfer in a fluidized bed, a compact bed accompanied by a large gas residence time is desirable.

Table 4. Effect of initial bed height on the predicted heat transfer coefficient

H_{mf} (m)	h_{sg} (W/m^{3}K)	h_{exp} (m)	$\delta=(H_{exp}-H_{mf})/H_{mf}$ (-)	$\alpha_{g,ave}$ (-)	t_{res} (s)
0.45	1 007 000	0.74	0.64	0.62	1.04
0.30	672 185.19	0.51	0.7	0.64	0.74
0.15	337 393.47	0.28	0.87	0.69	0.44

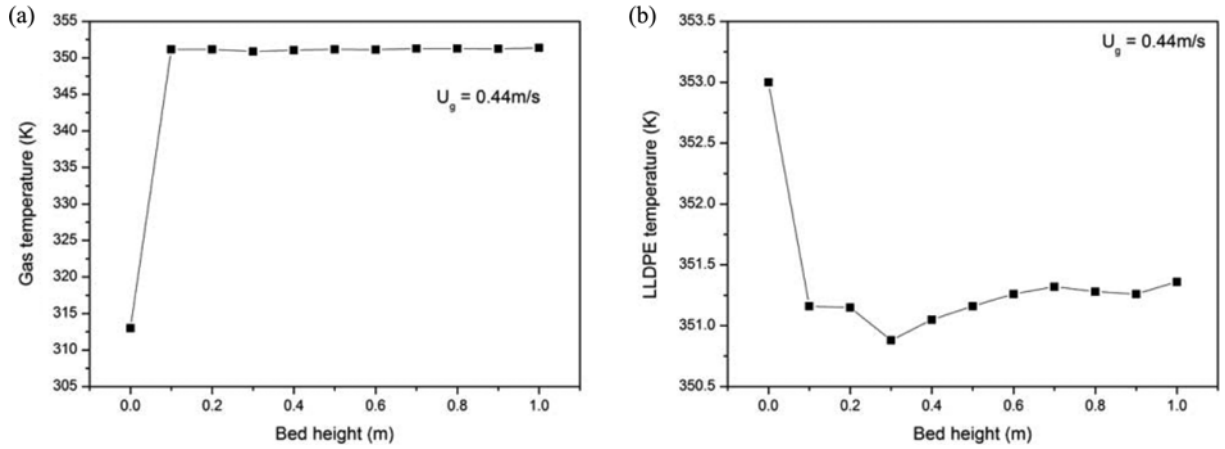

Fig. 14. (a) Temperature profile in Gas phase, (b) temperature profile in solid phase.

8. Temperature Profile of Gas and Solid Phase

In the present work the gas enters the bed at a temperature of 313 K and the solids are initially at 353 K, representing typical temperatures in a polymerization reactor [51]. Fig. 14(a) and Fig. 14(b) show the temperature profiles of the gas phase and solid phase after 20 seconds of simulations and at a superficial gas velocity of 0.44 m/s. Fig. 13(a) shows that the gas is rapidly heated to about 351 K, showing that the temperature of the gas follows the temperature of the particle. Thus, the temperature gradient is greatest at the inlet to the bed due to the large temperature driving force, i.e., the temperature difference between the two phases.

Van Heerden et al. [52] proposed an equation to calculate the thermal relaxation time, τ_g, in a fluidized bed which is the time required to establish a stationary gradient between the solid and gas phase and is given by:

$$\tau_g = \frac{2.3\rho_g c_{pg} d_s^2}{36\kappa_{g,0}} \tag{3}$$

Substitution of data into the above equation yields a thermal relaxation time of 359 μs; multiplying this value with a velocity of 0.44 m/s gives a distance of 0.0158 cm. Thus, a stationary gradient is established instantaneously at the bottom of the bed very close to the distributor; meanwhile simulations as shown by the temperature profile of the gas phase show that a stationary gradient is established within 0.1 m.

CONCLUSIONS

Simulations of interphase heat transfer in a gas solid fluidized bed have been performed using the Euler-Euler approach. An assessment of drag models shows that all drag models show a similar trend in the interphase heat transfer profile in the bed. Thus we can conclude that the drag models used do not have a significant effect on the predicted transfer coefficients. The large heat transfer rates in the bed are strongly influenced by the large specific interfacial areas rather than the particle-to-gas heat transfer coefficient, which is low. Care must be taken in specification of wall boundary conditions, especially the specularity coefficient, which significantly influences the heat transfer coefficient profile in the bed. Fluctuations of the interphase heat transfer coefficient are closely linked to the bubble motion in the bed. With an increase in the initial bed height, an increase in the heat transfer coefficient is observed. An increase in the superficial gas velocity leads to an appreciable increase in the heat transfer coefficient. With the reduction in the particle size, an increase in the heat transfer coefficient is observed together with an increase in the expansion of the bed. The temperature profiles of the gas phase and solid phase shows that thermal equilibrium is reached instantaneously close to the gas distributor. Thus our study has demonstrated that CFD is a powerful tool capable of capturing the complex heat transfer process in gas solid fluidized beds and is a useful tool in the design and scale up of fluidized bed reactors.

ACKNOWLEDGEMENTS

The authors sincerely wish to thank the financial support provided by The Project of National Natural Science Foundation of China (21236007) and National Basic Research Program of China (2012CB720500).

NOMENCLATURE

C_D : particle drag force coefficient [-]
c_p : specific heat capacity at constant pressure [J/kg·K]
d_s : mean particle diameter [m]
g : acceleration due to gravity [m/s^2]
h : fluid-particle heat transfer coefficient [W/m^2·K]
h_{sg} : interphase heat transfer coefficient [W/m^3·K]
H : enthalpy [J/kg]
Nu : Nusselt number [-]
p : pressure [pa]
Pr : Prandtl number
Re_s : particle Reynolds number [-]
t : time [s]
t_{res} : gas residence time [s]
T : temperature [K]
U_g, u : superficial gas velocity [m/s]
$u_{s,slip}$: slip velocity of particle at the wall [m/s]
$u_{s,w}$: tangential velocity of the particle at the wall [m/s]
y : vertical coordinate [m]

Greek Letters

α : volume fraction [-]
$\alpha_{s,max}$: solid volume fraction at maximum packing [-]
β_{gs} : gas/solid momentum exchange coefficient [kg/m^{2}s]
ξ_s : bulk viscosity [kg/m·s]
δ : bed expansion ratio [-]
Θ_s : granular temperature [m^2/s^2]
Θ_w : granular temperature at the wall [m^2/s^2]
ϕ_p : specularity coefficient [-]
ρ : density [kg/m^3]
$\overline{\overline{\tau_k}}$: stress tensor of phase k [pa]
τ_g : thermal relaxation time [s]
κ : thermal conductivity [W/m·k]
γ_s : collisional dissipation of solid fluctuating energy [kg/m·s^3]
γ_w : collisional dissipation of solid fluctuating energy at the wall [kg/m·s^3]

Subscripts and Superscripts

g : gas
k : phase k, solid or gas
s : solid phase

REFERENCES

1. H. S. Mickley and D. F. Fairbanks, *AIChE J.*, **1**, 374 (1955).
2. R. S. Brodkey, D. S. Kim and W. Sidner, *Int. J. Heat Mass Transfer*, **34**, 2327 (1991).
3. R. S. Figliola and D. E. Beasley, *Chem. Eng. Sci.*, **48**, 2901 (1993).
4. R. Yusuf, B. Halvorsen and M. C. Melaaen, *Int. J. Multiphase Flow*, **42**, 9 (2012).
5. J. Kuipers, W. Prins and W. Swaaij, *AIChE J.*, **38**, 1079 (1992).
6. M. Syamlal and D. Gidaspow, *AIChE J.*, **31**, 127 (1985).
7. D. Patil, J. Smit, M. Sint Annaland and J. Kuipers, *AIChE J.*, **52**, 58 (2006).
8. L. Armstrong, S. Gu and K. Luo, *Int. J. Heat Mass Transfer*, **53**, 4949 (2010).
9. C. Delvosalle and J. Vanderschuren, *Chem. Eng. Sci.*, **40**, 769 (1985).
10. J. Chang, G. Wang, J. Gao, K. Zhang, H. Chen and Y. Yang, *Powder Technol.*, **217**, 50 (2012).
11. Y. Yang, J. Yang, W. Chen and S. Rong, *Ind. Eng. Chem. Res.*, **41**, 2579 (2002).
12. D. Kunii and O. Levenspiel, *Fluidization engineering*, Butterworth-Heinemann Boston (1991).
13. Y. Kaneko, T. Shiojima and M. Horio, *Chem. Eng. Sci.*, **54**, 5809 (1999).
14. Y. Behjat, S. Shahhosseini and S. H. Hashemabadi, *International Communications in Heat and Mass Transfer*, **35**, 357 (2008).
15. M. Hamzehei, H. Rahimzadeh and G. Ahmadi, *Ind. Eng. Chem. Res.*, **49**, 5110 (2010).
16. X. Z. Chen, Z. H. Luo, W. C. Yan, Y. H. Lu and I. S. Ng, *AIChE J.*, **57**, 3351 (2011).
17. M. Syamlal and T. J. O'Brien, *AIChE Symposium Series*, **85**, 22 (1989).
18. M. Syamlal and T. J. O'Brien, *The derivation of a drag coefficient formula from velocity-voidage correlations*, US Department of Energy, Morgantown (1987).
19. D. Gidaspow, *Multiphase flow and fluidization: Continuum and kinetic theory descriptions*, Academic Press (1994).
20. J. Cao and G. Ahmadi, *Int. J. Multiphase Flow*, **21**, 1203 (1995).
21. S. Benyahia, M. Syamlal and T. J. O'Brien, *Powder Technol.*, **162**, 166 (2006).
22. C. Lun, S. Savage, D. Jeffrey and N. Chepurniy, *J. Fluid Mech.*, **140**, 223 (1984).
23. D. G. Schaeffer, *Journal of Differential Equations*, **66**, 19 (1987).
24. D. Ma and G. Ahmadi, *J. Chem. Phys.*, **84**, 3449 (1986).
25. D. Gunn, *Int. J. Heat Mass Transfer*, **21**, 467 (1978).
26. W. Ranz and W. Marshall, *Chem. Eng. Prog.*, **48**, 141 (1952).
27. N. Wakao, S. Kaguei and T. Funazkri, *Chem. Eng. Sci.*, **34**, 325 (1979).
28. A. Cybulski, M. J. Van Dalen, J. W. Verkerk and P. J. Van Den Berg, *Chem. Eng. Sci.*, **30**, 1015 (1975).
29. P. A. Nelson and T. R. Galloway, *Chem. Eng. Sci.*, **30**, 1 (1975).
30. B. Bird, W. Stewart and E. Lightfoot, *Transport phenomena, revised 2nd Ed.*, John Wiley & Sons, Inc. (2006).
31. N. G. Deen, S. H. L. Kriebitzsch, M. A. Van der Hoef and J. A. M. Kuipers, *Chem. Eng. Sci.*, **81**, 329 (2012).
32. J. Sun, Y. Zhou, C. Ren, J. Wang and Y. Yang, *Chem. Eng. Sci.*, **66**, 4972 (2011).
33. F. Taghipour, N. Ellis and C. Wong, *Chem. Eng. Sci.*, **60**, 6857 (2005).
34. P. Johnson and R. Jackson, *J. Fluid Mech.*, **176**, 67 (1987).
35. T. Li, J. Grace and X. Bi, *Powder Technol.*, **203**, 447 (2010).
36. R. Yusuf, M. C. Melaaen and V. Mathiesen, *Chem. Eng. Technol.*, **28**, 13 (2005).
37. S. Cloete, S. T. Johansen and S. Amini, *Powder Technol.*, **239**, 21 (2013).
38. C. Loha, H. Chattopadhyay and P. K. Chatterjee, *Chem. Eng. Sci.*, **75**, 400 (2012).
39. F. Vejahati, N. Mahinpey, N. Ellis and M. B. Nikoo, *Can. J. Chem. Eng.*, **87**, 19 (2009).
40. L. M. Armstrong, S. Gu and K. H. Luo, *Int. J. Multiphase Flow*, **36**, 916 (2010).
41. J. R. Grace, *Powder Technol.*, **113**, 242 (2000).
42. J. S. M. Botterill, *Fluid-bed heat transfer: Gas-fluidized bed behaviour and its influence on bed thermal properties*, Academic Press, London (1975).
43. C. Loha, H. Chattopadhyay and P. K. Chatterjee, *Particuology*, **11**, 673 (2013).
44. J. Tuot and R. Clift, *AIChE Symp. Ser.*, 78 (1973).
45. O.-a. Jaiboon, B. Chalermsinsuwan, L. Mekasut and P. Piumsomboon, *Powder Technol.*, **233**, 215 (2013).
46. A. P. Baskakov, V. G. Tuponogov and N. F. Filippovsky, *Powder Technol.*, **45**, 113 (1986).
47. O. Olaofe, M. Van der Hoef and J. Kuipers, *Chem. Eng. Sci.*, **66**, 2764 (2011).
48. X. Z. Chen, D. P. Shi, X. Gao and Z. H. Luo, *Powder Technol.*, **205**, 276 (2011).
49. J. Wang, C. Ren, Y. Yang and L. Hou, *Ind. Eng. Chem. Res.*, **48**, 8508 (2009).
50. S. Cloete, S. T. Johansen and S. Amini, *Powder Technol.*, **239**, 21 (2013).
51. M. L. DeChellis, J. R. Griffin and M. E. Muhle, US Patent, 5,405,922 (1995).
52. C. Van Heerden, A. Nobel and D. Van Krevelen, *Ind. Eng. Chem.*, **45**, 1237 (1953).

53. R. J. Hill, D. L. Koch and A. J. Ladd, *J. Fluid Mech.*, **448**, 213 (2001).
54. R. J. Hill, D. L. Koch and A. J. Ladd, *J. Fluid Mech.*, **448**, 243 (2001).
55. D. Ma and G. Ahmadi, *J. Chem. Phys.*, **84**, 3449 (1986).

APPENDIX A TWO FLUID MODEL AND CONSTITUTIVE RELATIONS

Mass conservation for phase k (k=g for gas and s for solid phase)

$$\frac{\partial}{\partial t}(\alpha_k\rho_k)+\nabla\cdot(\alpha_k\rho_k u_k)=0 \tag{A.1}$$

$$V_k=\int_V \alpha_k dV \tag{A.2}$$

Where

$$\sum_{k=1}^{n}\alpha_k=1 \tag{A.3}$$

Momentum conservation for solid phase

$$\frac{\partial}{\partial t}(\alpha_s\rho_s u_s)+\nabla\cdot(\alpha_s\rho_s u_s u_s)=\nabla\cdot\bar{\bar{\tau}}_s - \alpha_s\nabla P-\nabla P_s+\beta_{gs}(u_g-u_s)+\alpha_s\rho_s g \tag{A.4}$$

Momentum equation for gas phase:

$$\frac{\partial}{\partial t}(\alpha_g\rho_g u_g)+\nabla\cdot(\alpha_g\rho_g u_g u_g)=\nabla\cdot\bar{\bar{\tau}}_g - \alpha_g\nabla P-\beta_{gs}(u_g-u_s)+\alpha_g\rho_g g \tag{A.5}$$

Thermal energy conservation for solid phase

$$\frac{\partial}{\partial t}(\alpha_s\rho_s H_s)+\nabla\cdot(\alpha_s\rho_s u_s H_s)=-\nabla\cdot\alpha_s\kappa_s\nabla T_s+h_{sg}(T_g-T_s) \tag{A.6}$$

Thermal energy conservation for gas phase

$$\frac{\partial}{\partial t}(\alpha_g\rho_g H_g)+\nabla\cdot(\alpha_g\rho_g u_g H_g)=-\nabla\cdot\alpha_g\kappa_g\nabla T_s-h_{sg}(T_g-T_s) \tag{A.7}$$

Granular Temperature equation

$$\frac{3}{2}\left[\frac{\partial}{\partial t}(\alpha_s\rho_s\Theta_s)+\nabla\cdot(\alpha_s\rho_s u_s\Theta_s)\right]=(-P_s I+\tau_s):\nabla u_s-\nabla\cdot k_s\nabla\Theta_s-\gamma_s-3\beta_{gs}\Theta_s \tag{A.8}$$

CONSTITUTIVE EQUATIONS FOR INTERPHASE MOMENTUM TRANSFER

Syamlal O'Brien drag model [17]

$$\beta_{gs}=\frac{3}{4}\frac{\alpha_s\alpha_g\rho_g}{v_{rs}^2 d_s}C_D\left(\frac{Re_s}{v_{rs}}\right)|u_g-u_s| \tag{A.9}$$

$$C_D=\left(0.63+\frac{4.8}{\sqrt{Re_s/v_{rs}}}\right)^2,\quad Re_s=\frac{\rho_g|u_g-u_s|d_s}{\mu_g} \tag{A.10}$$

$$v_{rs}=0.5[A-0.06Re_s+\sqrt{(0.06Re_s)^2+0.12Re_s(2B-A)+A^2}] \tag{A.11}$$

Where

$$A=\alpha_g^{4.14}\text{ and }B=P\alpha_g^{1.28}\text{ for }\alpha_g\le 0.85 \tag{A.12}$$

$$A=\alpha_g^{4.14}\text{ and }B=\alpha_g^{Q}\alpha_g\text{ for }>0.85 \tag{A.13}$$

P=0.8 and Q=2.65

The adjusted Syamlal O'Brien drag function is obtained by calibrating the Syamlal O'Brien drag model such that it predicts the observed experimental minimum fluidization velocity. This is achieved by adjusting the parameters P and Q above using a Microsoft Excel spreadsheet.

Gidaspow drag model [19]

$$\beta_{gs}=\frac{3}{4}C_D\frac{\alpha_s\alpha_g\rho_g|u_g-u_s|}{d_s}\alpha_g^{-2.65}\text{ for }\alpha_g>0.8 \tag{A.14}$$

$$\beta_{gs}=150\frac{\alpha_s^2\mu_g}{\alpha_g d_s^2}+1.75\frac{\alpha_g\rho_g|u_g-u_s|}{d_s}\text{ for }\alpha_g\le 0.8 \tag{A.15}$$

$$c_D=\frac{24}{\alpha_g Re_s}[1+0.15(\alpha_g Re_s)^{0.687}],\ Re_s<1000 \tag{A.16}$$

$$c_D=0.44,\ Re_s>1000 \tag{A.17}$$

Cao Ahmadi drag model [20]

$$\beta_{gs}=\frac{18\mu_g\alpha_s}{d_s}\frac{[1+0.1(Re_s)^{0.75}]}{(1-(\alpha_s/\alpha_{s,max}))^{2.5\alpha_{s,max}}} \tag{A.18}$$

Hill et al. drag model [53,54]

Unlike the other drag models which are empirical in nature, the Hill et al. drag model is based on detailed lattice Boltzmann simulations, thereby making it a kinetic theory based model. In the present work the modified Hill et al. model [21], which covers the full range of void fractions and Reynolds numbers encountered in fluidized beds, has been adopted and is presented below.

$$\beta_{gs}=18F\mu_g\alpha_g^2(1-\alpha_g)/d_s^2 \tag{A.19}$$

$$F=1+3/8Re_s,\ \ \alpha_s\le 0.01\text{ and }Re_s\le\frac{F_2-1}{(3/8-F_3)}$$

$$F=F_0+F_1Re_s^2,\ \alpha_s>0.01\text{ and }Re_s\le\frac{F_3+\sqrt{F_3^2-4F_1}(F_0-F_2)}{2F_1}$$

$$F=F_2+F_3Re_s\begin{cases}\alpha_s\le 0.01\text{ and }Re_s>\dfrac{(F_2-1)}{(3/8-F_3)}\\ \alpha_s>0.01\text{ and }Re_s>\dfrac{F_3+\sqrt{F_3^2-4F_1}(F_0-F_2)}{2F_1}\end{cases} \tag{A.20}$$

$$F_0=\begin{cases}(1-w)\left[\dfrac{1+3\sqrt{\alpha_s/2}+(135/64)\alpha_s\ln(\alpha_s)+17.14\alpha_s}{1+0.681\alpha_s-8.48\alpha_s^2+8.16\alpha^3}\right]\\ \quad+w\left[10\dfrac{\alpha_s}{(1-\alpha_s)^3}\right] & 0.01<\alpha_s<0.4\\ 10\dfrac{\alpha_s}{(1-\alpha_s)^3} & \alpha_s\ge 0.4\end{cases} \tag{A.21}$$

$$F_1=\begin{cases}\dfrac{\sqrt{2/\alpha_s}}{40} & 0.01<\alpha_s\le 0.1\\ 0.11+0.00051\exp(11.6\alpha_s) & \alpha_s>0.1\end{cases} \tag{A.22}$$

$$F_2=\begin{cases}(1-w)\left[\dfrac{1+3\sqrt{\alpha_s/2}+(135/64)\alpha_s\ln(\alpha_s)+17.89\alpha_s}{1+0.681\alpha_s-11.03\alpha_s^2+15.41\alpha^3}\right] & \\ \quad +w\left[10\dfrac{\alpha_s}{(1-\alpha_s)^3}\right] & \alpha_s<0.4 \\ 10\dfrac{\alpha_s}{(1-\alpha_s)^3} & \alpha_s\geq 0.4\end{cases} \tag{A.23}$$

$$F_3=\begin{cases}0.9351\alpha_s+0.03667 & \alpha_s<0.0953 \\ 0.0673+0.212\alpha_s+0.0232/(1-\alpha_s)^5 & \alpha_s\geq 0.0953\end{cases} \tag{A.24}$$

$$Re_s=\frac{(1-\alpha_s)\rho_g|u_g-u_s|d_s}{2\mu_g} \tag{A.25}$$

$$w=e^{(-10(0.4-\alpha_s)/\alpha_s)} \tag{A.26}$$

CONSTITUTIVE EQUATIONS BASED ON THE KINETIC THEORY OF GRANULAR FLOW

Solid phase stress tensor

$$\bar{\bar{\tau}}_s=\alpha_s\mu_s[\nabla u_s+(\nabla u_s)^T]+\alpha_s\left(\xi_s-\frac{2}{3}\mu_s\right)\nabla\cdot u_s\bar{\bar{I}} \tag{A.27}$$

Gas phase stress tensor

$$\bar{\bar{\tau}}_s=\alpha_g\mu_g[\nabla u_g+(\nabla u_g)^T]-\frac{2}{3}\alpha_g\mu_g(\nabla\cdot u_g)\bar{\bar{I}} \tag{A.28}$$

Solids pressure [22]

$$p_s=\alpha_s\rho_s[1+2(1+e)\alpha_s g_0]\Theta_s \tag{A.29}$$

Bulk solid viscosity [22]

$$\xi_s=\frac{4}{3}\alpha_s\rho_s d_s g_0(1+e)\sqrt{\frac{\Theta_s}{\pi}} \tag{A.30}$$

Shear viscosity of solids

$$\mu_{s,kin}=\frac{10\rho_s d_s\sqrt{\pi\Theta_s}}{96\alpha_s(1+e)g_0}\left[1+\frac{4}{5}(1+e)g_0\alpha_s\right]^2 \tag{A.31}$$

Kinetic viscosity, $\mu_{s,kin}$ [19]

$$\mu_{s,kin}=\frac{10\rho_s d_s\sqrt{\pi\Theta_s}}{96(1+e)g_0}\left[1+\frac{4}{5}(1+e)g_0\alpha_s\right]^2 \tag{A.32}$$

Collisional viscosity, $\mu_{s,col}$ [19]

$$\mu_{s,col}=\frac{4}{5}\alpha_s^2\rho_s d_s g_0(1+e)\sqrt{\frac{\Theta_s}{\pi}} \tag{A.33}$$

Frictional viscosity $\mu_{s,fr}$ [23]

$$\mu_{s,fr}=\frac{p_s\sin\phi}{2\sqrt{I_{2D}}} \tag{A.34}$$

Where

ϕ is the internal angle of friction and I_{2D} is the second invariant of the deviatoric stress tensor.

Collisional dissipation of solid particle fluctuating energy [22]

$$\gamma_s=\frac{12(1-e)g_0}{d_s\sqrt{\pi}}\rho_s\alpha_s^2\Theta_s^{3/2} \tag{A.35}$$

Radial distribution function [55]

$$g_0=\frac{1+2.5\alpha_s+4.5904\alpha_s^2+4.515439\alpha_s^3}{\left[1-\left(\dfrac{\alpha_s}{\alpha_{s,max}}\right)^3\right]^{0.67802}} \tag{A.36}$$

JOHNSON AND JACKSON BOUNDARY CONDITIONS [34]

$$u_{s,w}=-\frac{6\mu_s\alpha_{s,max}}{\pi\phi_p\rho_s g_0\sqrt{3\Theta_s}}\frac{\partial u_{s,w}}{\partial n} \tag{A.37}$$

$$\Theta_w=-\frac{\kappa_s\Theta_s}{\gamma_w}\frac{\partial\Theta_w}{\partial n}+\frac{\sqrt{3}\pi\phi_p\alpha_s u_{s,slip}^2 g_0\Theta_s^{3/2}}{6\alpha_{s,max}\gamma_w} \tag{A.38}$$

Where

$$\gamma_w=\frac{\sqrt{3}(1-e_w^2)\alpha_s\rho_s g_0\Theta_s^{3/2}}{4\alpha_{s,max}} \tag{A.39}$$

CONSTITUTIVE EQUATIONS FOR THERMAL ENERGY BALANCE

The volumetric interphase heat transfer coefficient is obtained by multiplying the specific interfacial area of a spherical particle and the fluid particle heat transfer coefficient giving us the following equation:

$$h_{sg}=\frac{6\alpha_s h}{d_s} \tag{A.40}$$

Where h is the fluid particle heat transfer coefficient given by

$$h=\frac{Nu\cdot\kappa_{g,o}}{d_s} \tag{A.41}$$

Where Nu is the Nusselt number given by

$$Nu=(7-10\alpha_g+5\alpha_g^2)(1+0.7Re_s^{0.2}Pr^{1/3}) +(1.33-2.4\alpha_g+12\alpha_g^2)Re_s^{0.7}Pr^{1/3} \tag{A.42}$$

Where

$$Pr=\frac{\mu_g c_{p,g}}{\kappa_{g,o}} \tag{A.43}$$

Phase thermal conductivities

An expression for the effective thermal bed conductivity which consists of the gas phase conductivity and solid phase conductivity was derived by Kuipers et al. [5] and has been implemented in our model. The gas phase and solid phase conductivities are given by:

$$\kappa_g=\frac{(1-\sqrt{1-\alpha_g})\kappa_{g,o}}{\alpha_g} \tag{A.44}$$

$$\kappa_s=\frac{(\beta A+(1-\beta)K)\kappa_{g,o}}{\sqrt{1-\alpha_s}} \tag{A.45}$$

Where

$$K=\frac{2}{1-\frac{B}{A}}\left[\frac{A-1}{\left(1-\frac{B}{A}\right)^2}\frac{B}{A}\ln\frac{A}{B}-\frac{B-1}{1-\frac{B}{A}}-0.5(B+1)\right] \quad (A.46)$$

$$A=\frac{\kappa_{s,o}}{k_{g,o}}$$

$$B=1.25\left(\frac{1-\alpha_g}{\alpha_g}\right)^{10/9} \quad (A.47)$$

$$\beta=7.26\times10^{-3} \quad (A.48)$$

K is the effective thermal conductivity of a cylinder. This cylinder consists of one particle and the fluid phase.

β is the ratio of the particle contact area to the particle surface area

B is the factor of deformation